Photobleaching as a tool to measure the local strain field in fibrous membranes of connective tissues

Charles Jayyosi, Guillaume Fargier, Michel Coret, Karine Bruyère-Garnier

Photobleaching as a tool to measure the local strain field in fibrous membranes of connective tissues

C. Jayyosi [a,*], G. Fargier [b], M. Coret [c], K. Bruyère-Garnier [a]

[a] Université de Lyon, F-69622 Lyon;IFSTTAR, LBMC, UMR-T9406; Université Lyon 1, France
[b] Plateforme IVTV, CNRS, 36 Avenue Guy de Collongue, Bâtiment G8, 69134 Ecully Cedex, France
[c] LUNAM Université, GEM, UMR CNRS 6183, Ecole Centrale de Nantes, Université de Nantes, France

Connective tissues are complex structures which contain collagen and elastin fibers. These fiber-based structures have a great influence on material mechanical properties and need to be studied at the microscopic scale. Several microscopy techniques have been developed in order to image such microstructures; among them are two-photon excited fluorescence microscopy and second harmonic generation. These observations have been coupled with mechanical characterization to link microstructural kinematics to macroscopic material parameter evolution. In this study, we present a new approach to measure local strain in soft biological tissues using a side-effect of fluorescence microscopy: photobleaching. Controlling the loss of fluorescence induced by photobleaching, we create a pattern on our sample that we can monitor during mechanical loading. The image analysis allows three-dimensional displacements of the patterns at various loading levels to be computed. Then, local strain distribution is derived using the finite element discretization on a four-node element mesh created from our photobleached pattern. Photobleaching tests on a human liver capsule have revealed that this technique is non-destructive and does not have any impact on mechanical properties. This method is likely to have other applications in biological material studies, considering that all collagen–elastin fiber-based biological tissues possess autofluorescence properties and thus can be photobleached.

Keywords:
Photobleaching
Strain measurement
Multiphoton microscopy
Collagen
Elastin

1. Introduction

The study of soft biological tissue behavior is of particular interest in biomechanics, mainly because of its use for modeling purposes in various fields such as road safety and biomedical applications. At the macroscale, many mechanical tests have been put in place to assess biological material properties. For fibrous connective membranes, different experiments enable us to investigate their global behavior, calculating the failure stresses, apparent modulus and global strain [1–5].

However, there is a much more limited understanding of connective tissues micromechanics, and how the fiber composite structure reacts to loading and provides such mechanical behaviors. A few studies, mostly about tendons, have been conducted in order to investigate the changes in the microstructure during mechanical loading. They address fundamental questions about material characterization and give useful details about cellular strain environment. Screen and colleagues conducted a series of experiments in which they monitored the displacement of cell nuclei in tendons submitted to uniaxial tensile testing, to compute local strain of collagen fibers and understand the tendon extension mechanism [6–8]. Sasaki and Odajima [9] also worked on explaining tendon extension, linking it to different behaviors of collagen fibers at different scales, down to the molecular scale. More recently, Houssen et al. [10] performed uniaxial tensile tests on rat tail tendon and observed microstructure reorganization during loading, using second harmonic generation (SHG) signals from collagen fibers. Keyes et al. investigated vascular tissues behavior from a microstructural point of view, developing a pressure loading device and using multiphoton microscopy [11,12]. Such studies provide a brand new insight into natural material design and allow understanding on how fiber composite structures influence the macroscopic behavior.

In order to perform such investigation of soft biological tissue microstructures, many imagery techniques have been used. Among them, we find X-ray diffraction [9,13,14], polarized light [15,16], SHG [10], confocal microscopy [6,7,17,18], and a combination of SHG and two-photon excited fluorescence (TPEF) with multiphoton microscopy [11,12,19–22].

* Corresponding author. Tel.: +33 478656861.
E-mail address: charles.jayyosi@ifsttar.fr (C. Jayyosi).

Fluorescence microscopy is now well established as a valuable tool to observe the microstructure soft biological tissues. It has been widely used on many connective tissues, since their main components – collagen and elastin – have autofluorescence properties. Indeed, those two kinds of fibers each have several fluorophores [23–25], which allow their direct observation when excited at a specific wavelength, without requiring the use of specific fluorescent markers. Unfortunately, emission spectra of collagen and elastin overlap significantly, preventing them from being distinguished after excitation at the same wavelength [26].

On the other hand, collagen has a molecular organization that generates second harmonics [10,21,27]. Therefore it can be observed with multiphoton microscopy at precisely half the excitation wavelength. Considering those properties, it is thus possible to observe collagen and elastin fibers, and distinguish between them, by separating the TPEF and SHG signals, which show elastin and collagen, respectively. Some studies have already used those techniques to image collagen and elastin fibers simultaneously using a single two-photon excitation microscope [11,21,22].

One of the usual drawbacks of fluorescence microscopy is photobleaching. This phenomenon induces a loss of fluorophore fluorescence, which implies a decrease of signal/noise ratio and thus reduces the quality of the images [28,29]. Briefly, during the excitation of the fluorophore, molecules undergo permanent structural changes by reacting and creating covalent bonds with other species, especially oxygen. These changes often lead to an irreversible loss of fluorescence [30,31]. Photobleaching mechanisms are still not fully understood; however, many studies have focused on the factors enhancing this usually disruptive phenomenon. Among the most influential factors that have been reported are the specific fluorophore considered, the exciting photon flow intensity, the irradiation duration, the oxygen concentration and, more globally, the environment nature [30,32–36].

However, some microscopy techniques take advantage of the loss of fluorescence, such as fluorescence recovery after photobleaching, which allows the measurement of flow parameters such as the diffusion coefficient or the molecular speed [37,38]. Fluorescence localization after photobleaching is another technique, developed by Dunn et al. [39], which uses photobleaching to tag and track molecules. Cheng and Screen [40] proposed the use of photobleaching via classic confocal microscopy, to assess local strain in tendons after staining with fluorescent markers. They created lines of photobleaching, resulting in a grid on which they measured several parameters to characterize the local strain.

There are several differences between photobleaching induced by one- or multi-photon excitation. Indeed, considering that multi-photon excitation requires a much more powerful intensity excitation than one-photon excitation, photobleaching is stronger in TPEF [31,41]. With TPEF, photobleaching is also more localized, due to the confinement of excitation to a limited focal volume. Thus, TPEF provides limited photodamage within the sample and allows a more accurate control of the photobleached area borders [31].

Overall, photobleaching is a rather poorly understood phenomenon and, to our knowledge, no study has investigated its impact on the mechanical properties of biological tissues.

With the view of modeling human abdominal organs, we focus on the study of liver capsule mechanical behavior. As mentioned previously [11,12,20], in order to study the contribution of microstructure to the mechanical behavior of fibrous connective tissues at the macroscale, standard mechanical loading associated with the observation of fibers by TPEF and SHG offers a great potential. Moreover, it is important to assess the strain field at the microscale in such mechanical analysis, and the use of TPEF and SHG to this end is rarely reported. Only Screen and Evans have applied a finite element modeling approach using cells as markers to compute a strain field [8].

Using the same approach as Screen and Evans [8], we propose the use of photobleaching to create markers for a strain field measurement. The aim of this paper is first to demonstrate that this technique is non-destructive and does not affect a priori mechanical properties, and secondly to show the feasibility of the method to measure local strain field.

2. Materials and methods

2.1. Sample preparation

Human liver capsules were removed from a liver of post mortem human subject from the Department of Anatomy of the University of Rockefeller (DUAR, Lyon, France) through the French voluntary corpse donation to Science program. The capsule was delicately removed using a syringe and water to create a hematoma, then cut into dog-bone-shaped samples using a die cutter, giving a 45 mm length and a 6 mm section. Fig. 1a shows one of our sample's geometry. The dog-bone shape was initially chosen to investigate rupture behavior, which is not presented in this paper. Samples ($n = 4$) were stored at 4 °C until testing, which was performed within 2 days after preparation, so that the samples were never frozen. They were kept hydrated in saline solution until testing.

2.2. Microstructural observation

A two-photon excitation microscope (NIKON, A1R MP PLUS®) was used to observe the liver capsule microstructure. The excitation wavelength was set at 850 nm, which was specifically chosen as it is slightly above the values reported in the literature – 780 nm in Keyes et al. [11], 800 nm in Zoumi et al. [22] – to avoid collagen autofluorescence by exciting outside its excitation spectrum while exciting elastin at the high end of its spectrum. Second harmonic generated light from collagen and autofluorescent light from elastin were collected through two chanels using two filters, of 400–492 and 500–550 nm, respectively. The image field of view was $507 \times 507\ \mu m^2$, with a scan speed of 2 s per image and a resolution of 0.99 μm per pixel. To observe the changes along the entire thickness of the capsule, we imaged stacks of ~60–80 μm, depending of the capsule thickness, with one picture every 1 μm.

2.3. Definition of photobleaching conditions

To define the excitation parameters for photobleaching, and to study the potentially destructive effect of photobleaching, we made a test grid of photobleached squares with varying laser power and exposure time (Fig. 2). We computed total fluence, i.e. the total energy received per unit area for comparison. We started with low photobleaching at $53\ J\ mm^{-2}$ until very strong photobleaching at $2130\ J\ mm^{-2}$.

2.4. Grid of photobleaching for strain field measurement

In view of strain field measurement, a regular grid of photobleached squares was made in the field of view. This grid is composed of 16 squares (4×4), with sides of 20 μm for each and with 40 μm spacing, giving a total grid of 200 μm × 200 μm. Photobleaching was achieved according to the conditions selected previously: power was 50% of total power source, which is 600 mW at 850 nm for the laser considered; exposure time was set to 4 s per slice and the scanning irradiation was repeated three

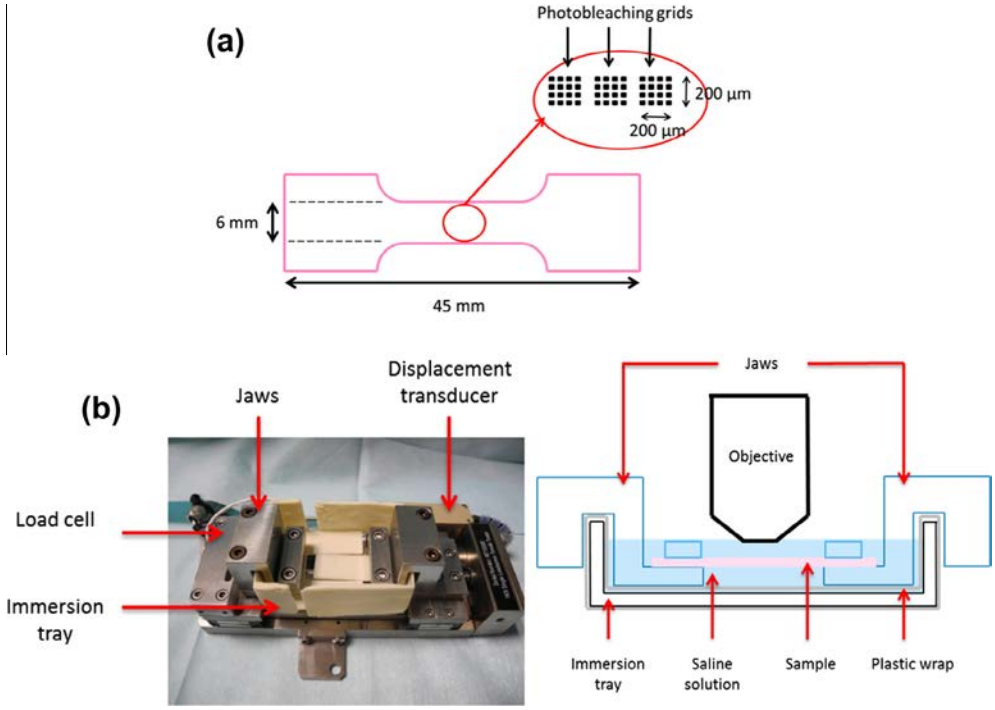

Fig. 1. (a) Description of sample geometry with positions of photobleaching grids. (b) Experimental setup. The custom-built immersion tray is put on the in situ micro tensile stage (DEBEN, UK). Immersion tray is in two parts to follow jaw displacements. Waterproofness is achieved by plastic wrap.

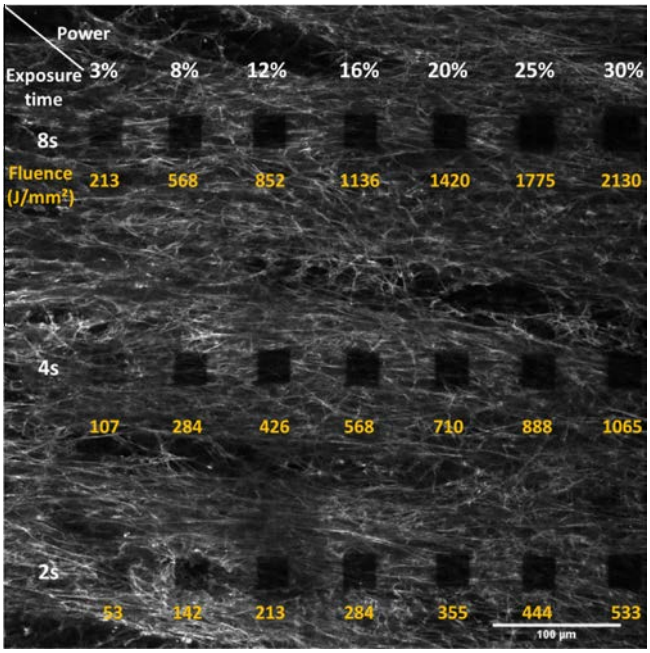

Fig. 2. Photobleached test grid as it appears on the fluorescence channel. Horizontally are different laser powers from 3% to 30% of total power source (600 mW). Vertically are different exposure times varying from 2 s to 8 s.Test square dimensions are 26 µm × 26 µm. Total fluence per photobleached square is computed (as power × exposure time/square area) and shown in yellow.

times. The total fluence for this process was 90 J mm^{-2}, which was a reasonable choice resulting from a compromise between limited laser power/exposure time – to prevent laser damage to the sample – and good contrast for the photobleached squares.

This process was performed in two distinct planes, spaced by ∼20 µm, to allow strain measurement along the thickness direction. We did not quantify the change in total thickness of the samples because the upper and lower limits of our tissue are difficult to identify with great precision. Indeed, depending on the gain/offset settings, the identification of the first and last planes where we monitor a signal varies and therefore we cannot get a good estimation of the sample total thickness. Following the position evolution of the two photobleached planes, we measured strain in the thickness direction. With such spacing between the two planes, we did not notice an impact of the depth of the focal plane on the intensity of photobleaching.

2.5. Mechanical loading

To perform uniaxial tensile testing, we used an in situ micro tensile stage (DEBEN, UK). This stage is equipped with a 150 N load cell and a displacement transducer. As the two jaws are mobile, we chose a region of interest (ROI) close to the middle of the sample so that it did not move too much during loading to ensure imaging of the same ROI during testing. However, there was a limited displacement of the ROI which needed repositioning that we performed thanks to the photobleached grid. An immersion tray, as well as custom-built jaws, was designed to perform these tests in a hydrated environment. Fig. 1b shows the experimental setup. Immersing the sample addresses several issues: it provides more realistic testing conditions, it ensures a water drop between the objective and the sample, and it is much easier to handle the liver capsule in a wet state. Loading was conducted at a speed of 1 mm min^{-1}. Samples were initially loaded to 0.05 N to ensure a flat initial state. Then, we performed a set of five loads/unloads between 0.05 N and 1 N, to remain in the quasi-linear section of the material behavior. We stopped at ∼15 min to image and photobleach our ROI, and performed another set of five identical cycles again. We repeated this loading pattern twice, changing the ROI each time to investigate the photobleaching effect on mechanical properties in the quasi-linear response of the material. We then conducted loading up to failure, stopping each 0.25 N to image

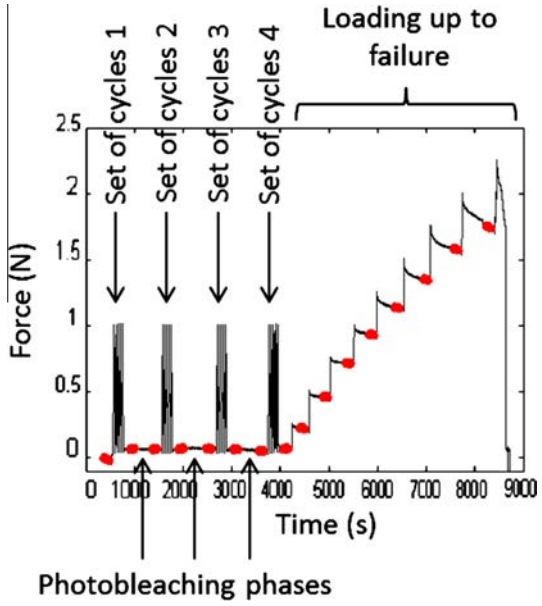

Fig. 3. Loading path (sample No. 4). It begins with four cycles of five loads/unloads between 0.05 N and 1 N. There are ≈15 min pauses between sets of cycles to perform photobleaching. Then the sample is loaded up to failure with pauses every 0.25 N for image acquisition of the photobleaching grid. Highlighted sections correspond to image acquisition.

one of our photobleached ROI. Fig. 3 presents the loading path, where sections corresponding to image acquisition for microstructural observation are indicated. From our force–displacement measurements, we computed engineering stress and engineering strain, dividing force and displacement by initial section and initial length, respectively.

2.6. Analysis of the influence of photobleached grids on macroscopic behavior

To assess the effects of photobleaching at the macroscopic scale, sets of loads/unloads before and after photobleaching were compared. The mean and standard deviation of distances between curves were computed by performing an orthogonal projection of the compared curve on the reference one.

Within a set of five loads/unloads, we compared each load/unload to the fifth one, to have a reference of acceptable curve distance measurement, assuming that the differences between loads/unloads within the same set of cycles are only due to normal re-organization of the structure.

We also compared each load/unload of every set of cycles to the fifth one of the first set of cycles – the one before photobleaching. Considering the fifth load/unload of the first set as a reference allowed us to avoid having to take into account all setup flaws, such as possible slippage or initial microcracks, and allowed us to compare cycles when they become repeatable. Then, considering the measurements within a same set as a reference for identical curves, we compared the measurements made between sets to gage the photobleaching effects.

2.7. Strain field measurement

Regarding local strain field measurement from the photobleached grid, the positions of the squares' centers were collected manually via image segmentation using ImageJ. The good contrast between photobleached squares and the rest of the image allows precise segmentation, down to 1 pixel accuracy. A Matlab script was developed to compute longitudinal, transverse and shear strains using the finite element method.

Using the coordinates of the squares' centers, a four-node element mesh of nine elements was made as seen in Fig. 4a. For each slice, longitudinal and transverse node displacements – u and v, respectively – were calculated forming a vector **U**.

Based on bilinear interpolation functions, the displacement gradient was calculated from the derivative of these functions presented here:

$$\begin{bmatrix} N_{1,x} \\ N_{1,y} \end{bmatrix} = \frac{1}{2A}\begin{bmatrix} -a + t*a \\ -a + s*a \end{bmatrix}, \begin{bmatrix} N_{2,x} \\ N_{2,y} \end{bmatrix} = \frac{1}{2A}\begin{bmatrix} a - t*a \\ -a - s*a \end{bmatrix},$$
$$\begin{bmatrix} N_{3,x} \\ N_{3,y} \end{bmatrix} = \frac{1}{2A}\begin{bmatrix} a + t*a \\ a + s*a \end{bmatrix}, \begin{bmatrix} N_{4,x} \\ N_{4,y} \end{bmatrix} = \frac{1}{2A}\begin{bmatrix} -a - t*a \\ a - s*a \end{bmatrix}$$

where $N_{k,x}$ is the derivative of the interpolation function with respect to x (longitudinal direction) and $N_{k,y}$ is the derivative with respect to y (transverse direction); s and t are the local coordinates and a and A are the side length and area of the reference square, as shown in Fig. 4b.

We calculated this displacement gradient at each of the four Gauss points defined by $[s,t] = [\pm 0.5774 \pm 0.5774]$.

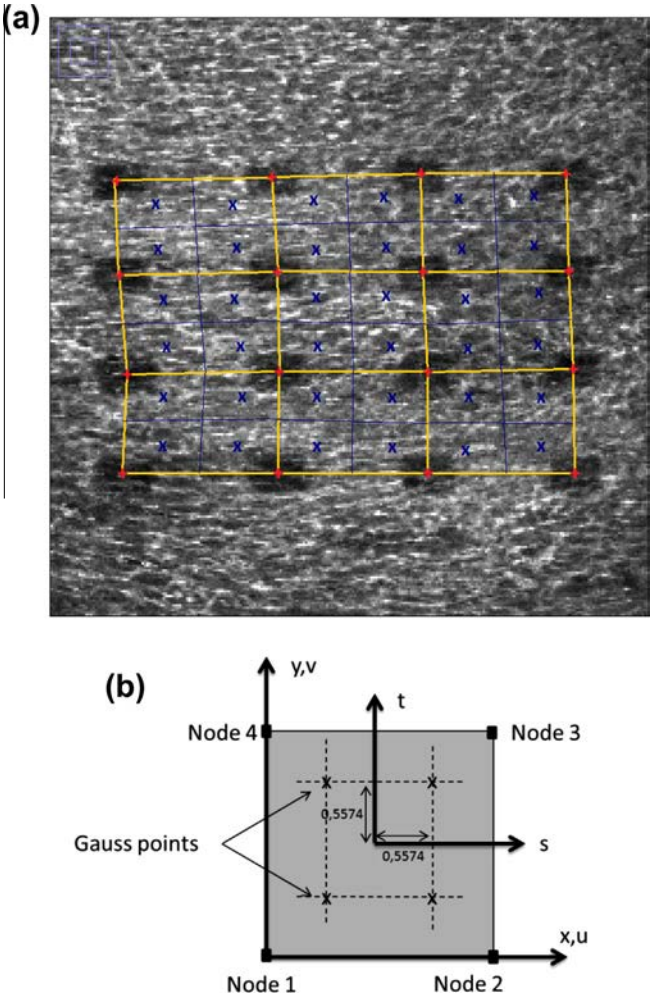

Fig. 4. (a) Four-node element mesh built from the photobleaching grid in a deformed state. The centers of photobleached squares (in red +) represent the nodes of the mesh, which is composed of nine elements. In blue x are the Gauss/integration points where the gradient of displacement is calculated. Therefore we compute four Green–Lagrange strain tensors per element and use a Matlab routine to color each quarter of the elements according to the associated value of strain. (b) Definition of Gauss points/integration points in the finite element mesh. (For interpretation of the references to colours in this figure legend, the reader is referred to the web version of this paper.)

From this gradient, we obtain the Green–Lagrange strain tensor by

$$E = \frac{1}{2}(\vec{g}rad(\vec{u}) + \vec{g}rad(\vec{u})^T + \vec{g}rad(\vec{u}).\vec{g}rad(\vec{u})^T)$$

Eventually, we computed four strain tensors per square, resulting in 36 strain tensors per slice. Considering that the x, y coordinates of photobleached squares do not change much from one slice to another, we computed the mean value between the two photobleached planes segmented for strain tensors in each square and used a Matlab routine for color representation.

This new method of strain measurement is an alternative to digital image correlation, which is usually used for large strain distribution analysis [42–44].

We computed Green–Lagrange strain in the thickness direction, based on the measurement of the distance between our two photobleached planes at each loading step, to get a first estimation of local strain in that direction.

3. Results

3.1. Definition of photobleaching conditions

Fig. 2 shows the test grid on one slice as it appears in the fluorescence channel with indicated fluence for each square. There is no apparent damage of the sample after the completion of the test grid with variable fluence. As photobleaching affects fluorescence but not the SHG signal, we can still monitor the collagen fibers after photobleaching via the SGH channel. For fluence under 890 J mm^{-2}, the SHG signal is still clearly present in the photobleached squares. It starts to disappear – which could correspond to a burnt hole – above this value, but not on every slice, which indicates that we have not reached the full destruction of the tissue, even with the highest value of fluence tested.

To obtain clear markers by photobleaching and to avoid any damage of the tissue, we choose parameters to obtain a fluence rate of 90 J mm^{-2} to perform the grid. Fig. 5 shows the photobleached grid before loading. With these conditions, we zoomed in on one photobleached square to assess qualitatively the effects of photobleaching on the geometry of the fibers' network and to detect a potential burnt area. Fig. 6 shows both the SHG (a) and fluorescence (b) channel of a zoom on a photobleached square. Image analysis reveals that we still detect a SHG signal in the square, showing that the collagen fibers have not suffered a priori from photobleaching and appear, structurally speaking, intact. The geometry of elastin fibers network does not appear modified either by this process, considering that, even if we lost some fluorescence, there is still some signal left that allows us to monitor parts of the fibers which appear to have kept their continuity, as seen in Fig. 6b. Besides, elastin fibers present around the square are not modified. We also repeated the zoom operation several times after loading to make sure that photobleaching does not modify the fibers' kinematics, observing qualitatively the behavior of collagen and elastin fibers. The extremities of elastin fibers, as seen on the borders of the photobleached squares, seem to have coherent kinematics with one another, as their displacements were correlated. Regarding collagen fibers, their behaviors were no different from what was previously observed.

3.2. Comparison of macroscopic mechanical behaviors after photobleaching

Fig. 7 presents an example of the first set of five cycles (a) and a set of five cycles after three photobleachings (b). The five cycles within a set show a high repeatability, as well as loads/unloads between different sets. Table 1 shows mean values of intercurve

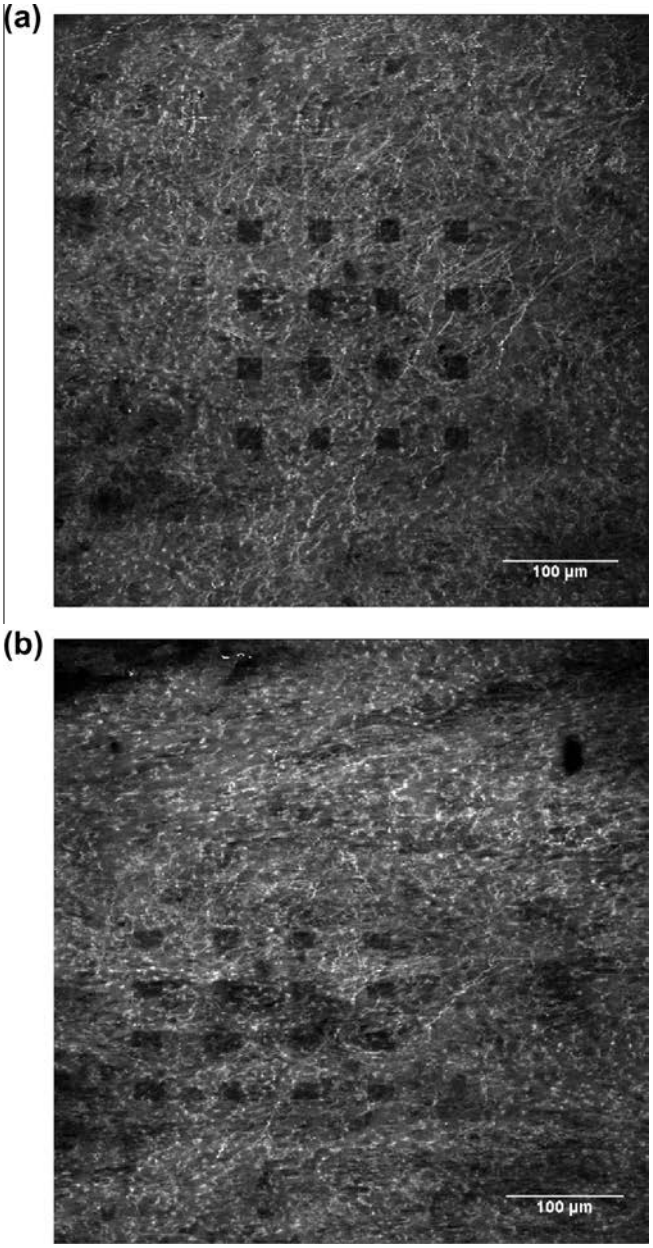

Fig. 5. Grayscale images of the human liver capsule as seen on the fluorescent channel of the two-photon excitation microscope for sample No. 4. (a) Photobleaching grid before loading (force level $F = 0.07$ N). Initial square dimensions are 20 µm × 20 µm with 40 µm spacing between them. (b) Photobleaching grid after loading (force level $F = 1.76$ N).

distances and the associated standard deviations. The "reference" line refers to the calculation of mean distance values between loads/unloads of a same set. Averaging the results among the different samples, we find a mean distance of 4.0 kPa (SD 0.7) and a standard deviation of 3.0 kPa (SD 5), which we consider as reference values for quasi-identical curves.

Except for the very first cycle of the first set – which takes into account initial setting flaws and irreversible phenomenon like a first fiber alignment in the loading direction – cycles are very much alike, as shown by the low values of both mean and standard deviation of curve distances with respect to reference values.

3.3. Local strain field measurement

Fig. 8 shows an example of strain field evolution during loading. The transverse strain far exceeds the longitudinal strain in absolute

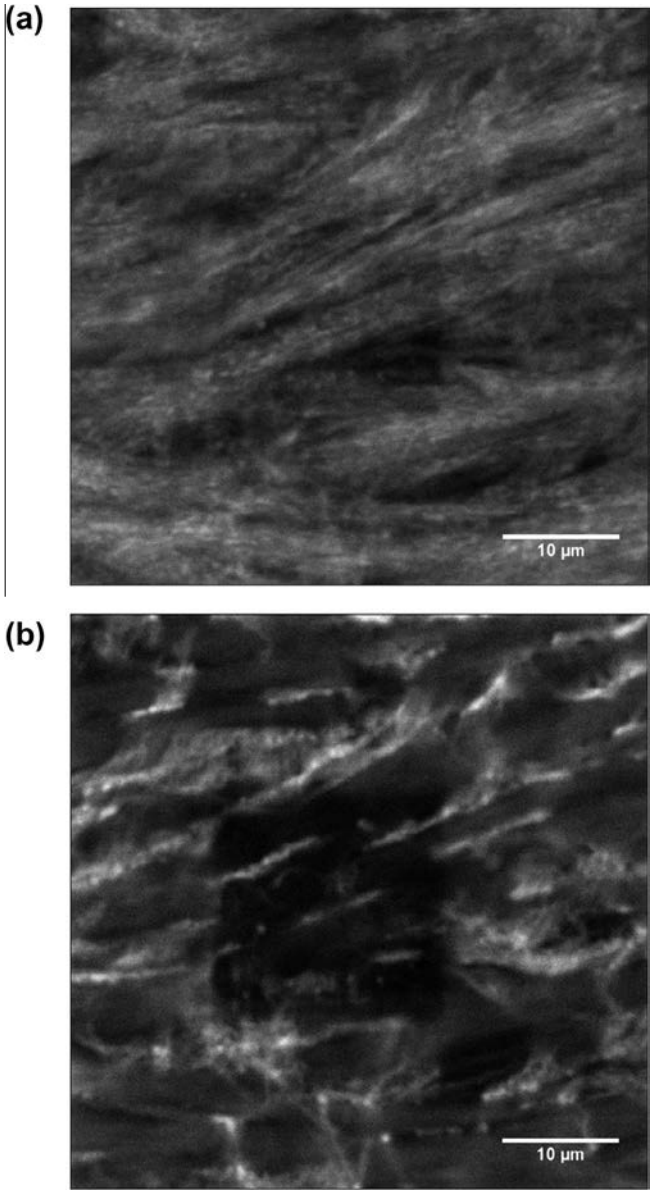

Fig. 6. Zoom (×10) on a photobleached square before loading (force level $F = 0.01$ N). Total field of view is 51.2 µm × 51.2 µm with a resolution of 0.05 µm per pixel. (a) SHG channel showing the collagen fibers. (b) Fluorescence channel showing mainly elastine fibers and the photobleached square.

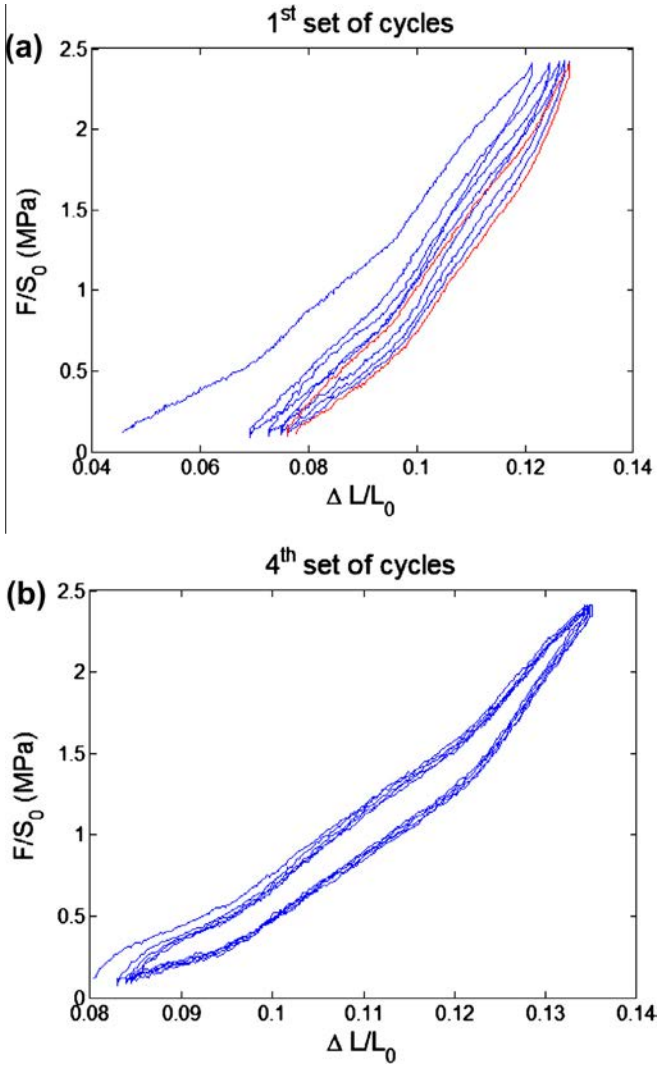

Fig. 7. (a) First set of five cycles (sample No. 4) of human liver capsule loading as seen on the engineering stress–strain curve. Loading is conducted between 0.05 N and 1 N at 1 mm min^{-1} speed. Every cycle of every set is compared to the fifth cycle of this set (shown in red). (b) Fourth set of five cycles showing the repeatability of the liver capsule engineering stress–strain behavior (sample No. 4).

value, with a maximum transverse strain at −0.311 (SD 0.066, $n = 4$), while maximum longitudinal strain is 0.216 (SD 0.061, $n = 4$). For shear strain, a great variability among the samples is observed.

Fig. 10 presents the compared evolution of global engineering strain with longitudinal local strain. We notice an identical trend for these two parameters but there is a random shift, more or less important depending on the sample, between the two curves. The differences between global and local strain vary from 1.1 to 40%, indicating that local strain might be very representative of global strain in some location or not at all in others.

Regarding computed strain in the thickness direction, E_{zz}, results were not satisfying. Fig. 11 shows E_{zz} evolution with loading for the four samples tested, and illustrates the high uncertainty of the measurements. To compute this strain accurately, we need to identify two distinguishable planes that we can spot on image stacks at each loading step. Unfortunately, our localized photobleaching does not mark a single plane but a stack of ~6 µm, so we cannot rely on that to identify the planes. Therefore, we note some particular structures that we can easily distinguish to ensure that we are considering the same planes each time.

Table 1
Average values and standard deviation of intercurve distances.

	Intercurve distances (kPa)	
	Average (Number of points≈600, Number of cycles = 5)	Standard deviation (Number of points≈600, Number of cycles = 5)
Reference	4.0 (SD = 0.7) ($n = 4$)	3.0 (SD = 0.5) ($n = 4$)
No photobleaching	5.1 (SD = 0.7) ($n = 4$)	3.5 (SD = 0.7) ($n = 4$)
One grid of photobleaching	4.3 (SD = 0.5) ($n = 4$)	2.7 (SD = 0.1) ($n = 4$)
Two grids of photobleaching	4.2 (SD = 0.4) ($n = 4$)	2.7 (SD = 0.1) ($n = 4$)
Three grids of photobleaching	4.8 (SD = 1.4) ($n = 4$)	2.8 (SD = 0.2) ($n = 4$)

Reference refers to distances within a same set of five cycles which are assumed to represent typical distances between very similar curves. Values are given with standard deviation with respect to intersample variability ($n = 4$). Average and standard deviation of intercurve distances are mean values calculated over ~600 points and averaged on the five cycles within the same set.

However, considering that, along with thickness, we have one image every 1 μm, and thus we cannot reach a great accuracy on the position of our considered planes. Thus we do not observe a clear trend in the E_{zz} variations, and the poor accuracy of our measurements hides a probable slight decrease that we observe during live imaging.

4. Discussion

The levels of fluence mentioned in this study are way above the values given in the literature for photobleaching experiments on collagen and elastin compounds reported by Marcu et al. [33]. This difference is because usually, in studies about photobleaching, one focuses on the first appearance of this phenomenon to detect and avoid it, whereas in our case we need a complete photobleaching of our squares for good contrast and easy segmentation. Moreover, the laser type impacts greatly on the fluence levels, and TPEF is more energetic and localized than classic confocal excitation [31,41]. Finally, the fluence levels also depend on the wavelength and material considered [33].

Even with the high power laser values considered, we did not observe any damage to the liver capsule. The presence of the

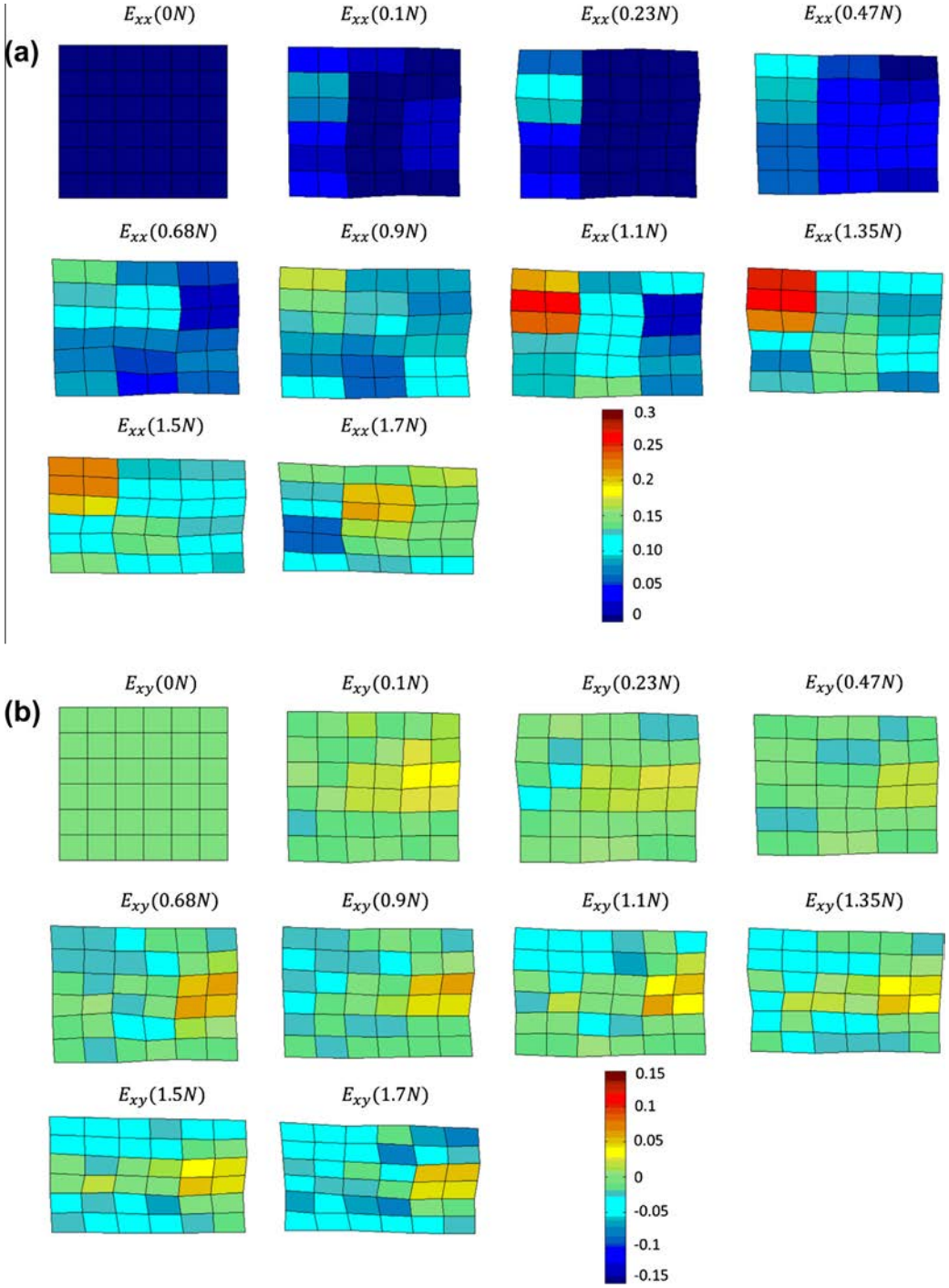

Fig. 8. Green–Lagrange strain field evolution during loading (sample No. 3) showing the heterogeneity of local strain in human liver capsule. Each image is associated to a level of loading indicated by the average force level measured during image acquisition. Each square represents the value of Green–Lagrange strain calculated at a specific Gauss point. (a) Longitudinal strain; (b) shear strain; (c) transverse strain; (d) norm ($||E|| = (E_{ij}\ E_{ij})^{1/2}$).

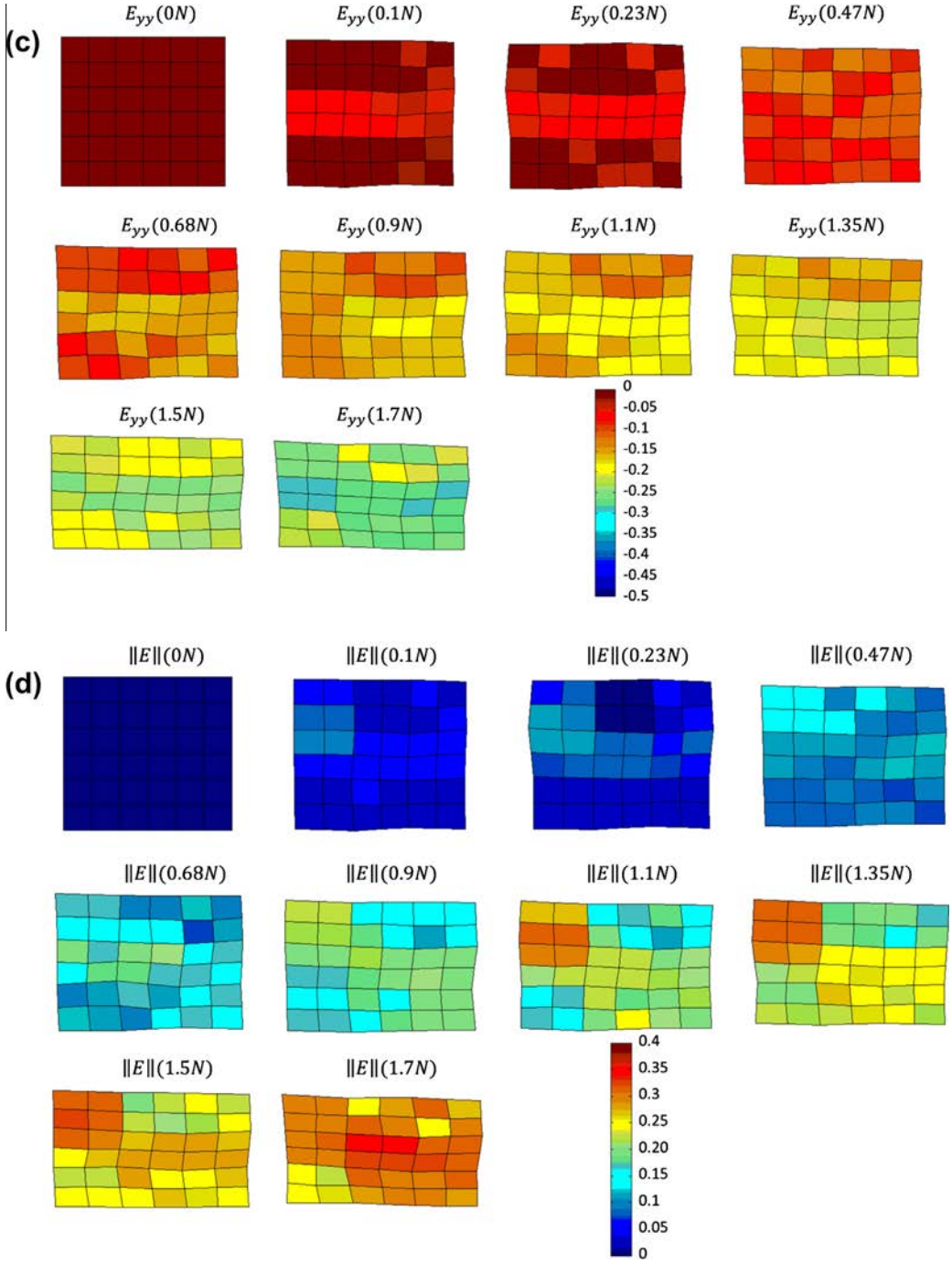

Fig. 8 (*continued*)

SHG signal in the photobleach squares indicates that collagen fibers are still clearly present in the photobleaching area. We can also assume that elastin fibers were not destroyed as well, even if they are no longer visible, considering that fibers on the very border of photobleached squares have not changed and do not seem burnt, cut or damaged. However, in some cases, the photobleached square appeared on the SHG channel because of the insufficient selectiveness of our filters. Indeed, the band pass of our SHG filter is too wide, and therefore we collect a small amount of autofluorescence in this channel, just enough for the photobleached square to be visible. Anyway, it appears that photobleaching does not affect the tissue integrity as we did not notice once the beginning of a rupture in any photobleached zone, which could have been the case if the laser had burnt holes in the tissue. Moreover, qualitative observation of the zoom of the photobleached squares reveals that the geometry of collagen fibers is not modified. We can reasonably assume that this is also the case for elastin fiber geometry, considering that fibers around squares are not affected and the fibers seem to have kept their continuity.

The comparison of cyclic tests reveals that global behavior is not modified by photobleaching, as the cycles did not change much after each photobleaching phase. The small discrepancy in cycle shape is due to setting adjustments, and vanishes after some cycles. Therefore, we did not observe any impact of photobleaching on global mechanical properties. This was not unexpected, considering the small volume affected by this phenomenon.

If we consider the effect of photobleaching at the local scale, mechanical damage of the tissue would also appear on a local strain

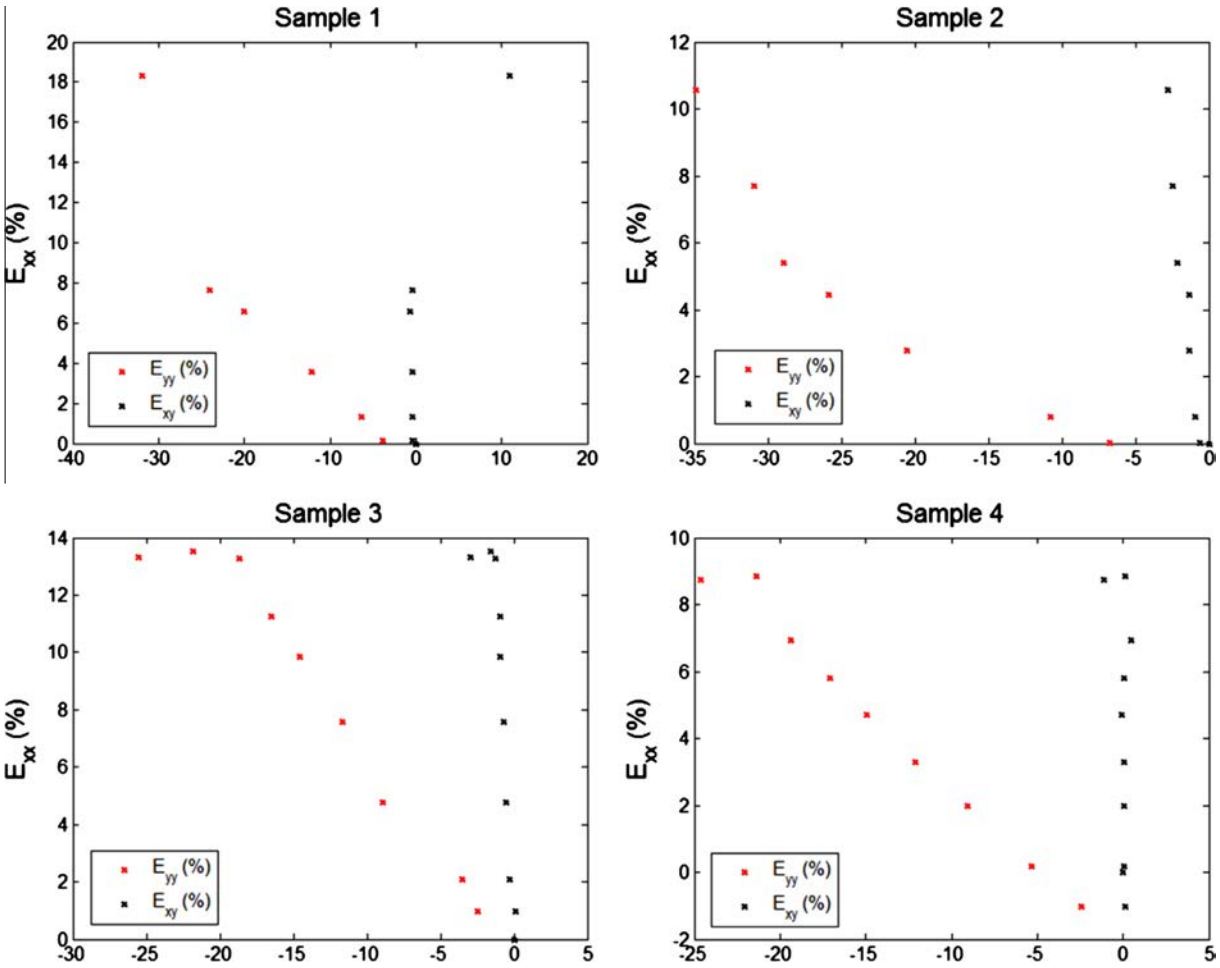

Fig. 9. Variation of mean longitudinal strain (E_{xx}) with respect to mean transverse strain (E_{yy} shown in red) and mean shear strain (E_{xy} shown in black) for the four samples tested. While shear strain does not vary much, transverse strain becomes greater than longitudinal strain in absolute value.

map analysis. Indeed, damage would induce systematic differences on strain within the grid between strain on the border and strain at the center. To evaluate possible trends on strain, we compute a norm of strain ($||E|| = (E_{ij}\ E_{ij})^{1/2}$), which is presented in Fig. 8d for sample No. 3. No particular trend was seen and, in particular, we did not notice a higher strain on the border of the grid, which would have been the case if the tissue had suffered mechanical damage.

With regard to local strain field measurements, we observed, on the four samples tested, that the transverse strain was greater than the longitudinal strain in absolute value, as shown in Figs. 8 and 9. This shows that structural effects might be predominant in the elongation process of the liver capsule. This concurs with previous findings about the tendon elongation mechanism, which is not entirely due to fiber elongation [6,9,10]. Screen et al. [6] highlighted the fact that tendon elongation is primarily due to fiber sliding, at different scales, while fiber elongation accounts for a small part of global extension. Fiber reorientation and uncrimping are also key factors in tendon extension [10]. It is likely that we find the same mechanisms at work with liver capsules, which, unlike tendons, where fibers are already more or less pre-aligned in the tendon axis, are far less organized, and present a "chaotic" network which induces many structural effects that are difficult to predict.

Therefore, those structural effects induce local changes of volume. Locally, the particular arrangement of fibers before stretching is much less organized. During loading, fibers align in one direction, and this reorganization induces an increase of fiber density in the considered volume. In fact, the volume can be reduced slightly because the spacing between fibers is reduced with reorganization due to structural effects. Previous studies [45,46] have reported the phenomenon of exudation of fluid from the extracellular matrix during loading of collagen fiber bundles, resulting in a loss of fluids of the structure that contributes to the reduction of interfibrillar space.

Moreover, shear strain values are quite heterogeneous among the samples. Depending on location, the fibers inside the ROI experience sliding one way or the other. Much like tendons [6], collagen fibers tend to slide from one to another where the link between them is the weakest. That explains why shear strain reaches important positive or negative values when the sliding occurs in the photobleached zone, or why in some cases shear strain barely differs from 0, when the link between collagen fibers is strong enough to prevent sliding.

As expected, local and global longitudinal strains do not match perfectly, as seen in Fig. 10. However, given the sample's dog-bone geometry, local strain should be higher than global strain, which is a trend that we do not observe in Fig. 10. Indeed, depending on the location of the ROI, fibers experience different elongation/sliding intensities, resulting in a heterogeneous local longitudinal strain throughout the sample which therefore does not match a homogeneous behavior.

For strain along thickness measurements, we cannot draw any conclusions considering the high uncertainty when we followed the two reference planes which are photobleached. However, this method remains valid and would only need a smaller z-step during

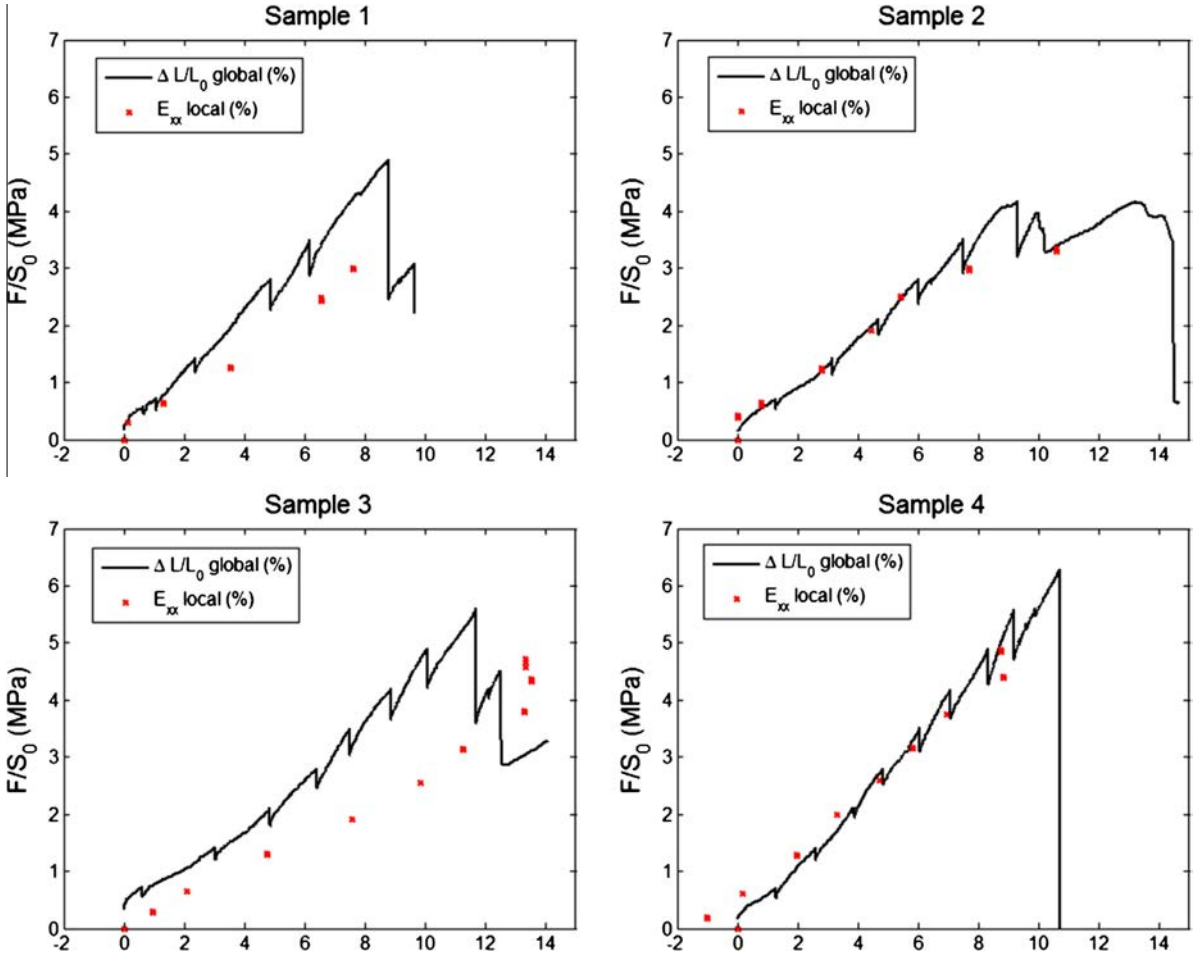

Fig. 10. Global/local longitudinal strain comparison on the four samples. E_{xx} local corresponds to the average value of local longitudinal strain over the photobleached grid calculated at the different loading level of image acquisition.

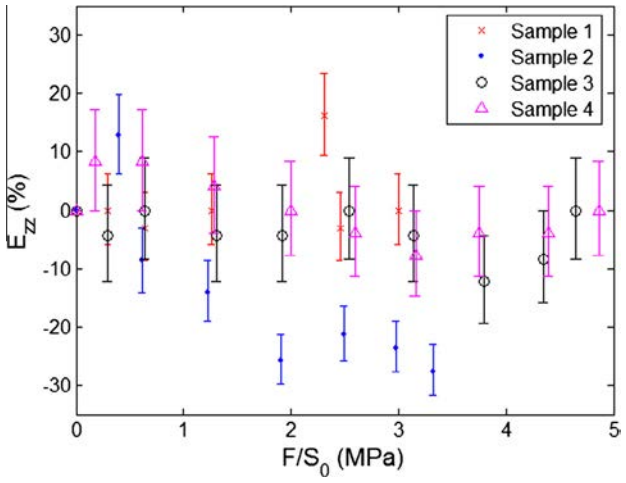

Fig. 11. Green–Lagrange strain evolution in the thickness direction for the four samples tested (error bars represent the uncertainty of the measurement) at the different levels of loading corresponding to image acquisition.

image acquisition. With this greater image density in the thickness direction, we could expect to reach a greater resolution down to the optical limit of the microscope. The main issue would be that a smaller z-step would lead to longer pauses during loading, with longer relaxation time and an important decrease in force measurement.

5. Conclusion

In this study, we presented a new method to measure local strain field in connective fibrous membranes. We demonstrated the validity of using photobleaching to create markers on this tissue, showing that it does not impact macroscopic mechanical properties or collagen fiber geometry, if performed at a certain fluence level. This technique is quite useful for studying fiber-based structures which have autofluorescent properties, which is the case for many biological tissues based on collagen–elastin fibers, such as skin, arterial walls, tendons or other connective membranes. It allows positioning intrinsic markers on those tissues, which can be used to various aims such as following a precise ROI during loading or measuring local strain in three dimensions, as is presented in this study. To have an insight into local strain field on such structures may allow an understanding of the contribution of microstructure to the macroscopic mechanical behavior of the tissue and to the damage and failure mechanisms. Such information is the starting point to develop structurally based models of materials behavior and can be used to help design or validate the behavior of engineered biomaterials.

Disclosures

None of the authors has any professional or financial conflict of interest.

Acknowledgements

The authors thank the IVTV (ANR-10-EQPX-06-01) team for its help during the imaging process.

This work was supported by the Programme Avenir Lyon Saint-Etienne (ANR-11-IDEX-0007) of Université de Lyon, within the program "Investissements d'Avenir" operated by the French National Research Agency (ANR).

Appendix A. Figures with essential colour discrimination

Certain figures in this article, particularly Figs. 1–4 and 7–11, are difficult to interpret in black and white. The full colour images can be found in the on-line version, at http://dx.doi.org/10.1016/j.actbio.2014.02.031.

References

[1] Brunon A, Bruyère-Garnier K, Coret M. Characterization of the nonlinear behaviour and the failure of human liver capsule through inflation tests. J Mech Behav Biomed Mater 2011;4(8):1572–81.
[2] Umale S, Deck C, Bourdet N, Dhumane P, Soler L, Marescaux J, et al. Experimental mechanical characterization of abdominal organs: liver, kidney & spleen. J Mech Behav Biomed Mater 2013;17:22–33.
[3] Perrini M, Bürzle W, Haller C, Ochsenbein-Kölble N, Deprest J, Zimmermann R, et al. Contractions, a risk for premature rupture of fetal membranes: a new protocol with cyclic biaxial tension. Med Eng Phys 2013;35(6):846–51.
[4] Ní Annaidh A, Bruyère K, Destrade M, Gilchrist MD, Otténio M. Characterization of the anisotropic mechanical properties of excised human skin. J Mech Behav Biomed Mater 2012;5(1):139–48.
[5] Stemper BD, Yoganandan N, a Pintar F. Methodology to study intimal failure mechanics in human internal carotid arteries. J Biomech 2005;38(12):2491–6.
[6] Screen HRC, Lee DA, Bader DL, Shelton JC. An investigation into the effects of the hierarchical structure of tendon fascicles on micromechanical properties. Proc Inst Mech Eng H 2004;218(2):109–19.
[7] Screen HRC. Investigating load relaxation mechanics in tendon. J Mech Behav Biomed Mater 2008;1(1):51–8.
[8] Screen HRC, Evans SL. Measuring strain distributions in tendon using confocal microscopy and finite elements. J Strain Anal Eng Des 2009;44(5):327–35.
[9] Sasaki N, Odajima S. Force–strain mechanism of collagen fibrils and relations of tendon at each level of structural. Science 1995;29(9):1131–6.
[10] Houssen YG, Gusachenko I, Schanne-Klein M-C, Allain J-M. Monitoring micrometer-scale collagen organization in rat-tail tendon upon mechanical strain using second harmonic microscopy. J Biomech 2011;44(11):2047–52.
[11] Keyes JT, Lockwood DR, Simon BR, Vande JP. Geest, Deformationally dependent fluid transport properties of porcine coronary arteries based on location in the coronary vasculature. J Mech Behav Biomed Mater 2013;17:296–306.
[12] Keyes JT, Haskett DG, Utzinger U, Azhar M, Vande JP. Geest, Adaptation of a planar microbiaxial optomechanical device for the tubular biaxial microstructural and macroscopic characterization of small vascular tissues. J Biomech Eng 2011;133(7):075001.
[13] Liao J, Yang L, Grashow J, Sacks MS. Molecular orientation of collagen in intact planar connective tissues under biaxial stretch. Acta Biomater 2005;1(1):45–54.
[14] Purslow PP, Wess TJ, Hukins DW. Collagen orientation and molecular spacing during creep and stress–relaxation in soft connective tissues. J Exp Biol 1998;201(Pt 1):135–42.
[15] Lake SP, Miller KS, Elliott DM, Soslowsky LJ. Effect of fiber distribution and realignment on the nonlinear and inhomogeneous mechanical properties of human supraspinatus tendon under longitudinal tensile loading. J Orthop Res 2009;27(12):1596–602.
[16] Lake SP, Miller KS, Elliott DM, Soslowsky LJ. Tensile properties and fiber alignment of human supraspinatus tendon in the transverse direction demonstrate inhomogeneity, nonlinearity, and regional isotropy. J Biomech 2010;43(4):727–32.
[17] Briones AM, González JM, Somoza B, Giraldo J, Daly CJ, Vila E, et al. Role of elastin in spontaneously hypertensive rat small mesenteric artery remodelling. J Physiol 2003;552(Pt 1):185–95.
[18] Boumaza S, Arribas SM, Osborne-Pellegrin M, McGrath JC, Laurent S, Lacolley P, et al. Fenestrations of the carotid internal elastic lamina and structural adaptation in stroke-prone spontaneously hypertensive rats. Hypertension 2001;21(1):1101–7.
[19] Raub CB, Unruh J, Suresh V, Krasieva T, Lindmo T, Gratton E, et al. Image correlation spectroscopy of multiphoton images correlates with collagen mechanical properties. Biophys J 2008;94(6):2361–73.
[20] Rubbens MP, Driessen-Mol A, Boerboom RA, Koppert MMJ, Van Assen HC, TerHaar Romeny BM, et al. Quantification of the temporal evolution of collagen orientation in mechanically conditioned engineered cardiovascular tissues. Ann Biomed Eng Jul. 2009;37(7):1263–72.
[21] Zoumi A, Yeh A, Tromberg BJ. Imaging cells and extracellular matrix in vivo by using second-harmonic generation and two-photon excited fluorescence. Proc Natl Acad Sci USA Aug. 2002;99(17):11014–9.
[22] Zoumi A, Lu X, Kassab GS, Tromberg BJ. Imaging coronary artery microstructure using second-harmonic and two-photon fluorescence microscopy. Biophys J 2004;87(4):2778–86.
[23] Deyl Z, Macek K, Adam M, Vancíková O. Studies on the chemical nature of elastin fluorescence. Biochim Biophys Acta 1980;625(2):248–54.
[24] Fujimori E. Changes induced by ozone and ultraviolet light in type I collagen. Bovine Achilles tendon collagen versus rat tail tendon collagen. Eur J Biochem 1985;152(2):299–306.
[25] Fujimoto D, Akiba K, Nakamura N. Isolation and characterization of a fluorescent material in bovine achilles tendon collagen. Biochem Biophys Res Commun 1977;76(4):1124–9.
[26] Richards-Kortum R, Sevick-Muraca E. Quantitative optical spectroscopy for tissue diagnosis. Annu Rev Phys Chem 1996;47:555–606.
[27] Campagnola PJ, Millard AC, Terasaki M, Hoppe PE, Malone CJ, Mohler WA. Three-dimensional high-resolution second-harmonic generation imaging of endogenous structural proteins in biological tissues. Biophys J 2002;82(1 Pt 1):493–508.
[28] Pawley J. Fundamental Limits in Confocal Microscopy. In: Pawley JB, editor. Handbook Of Biological Confocal Microscopy SE - 2. US: Springer; 2006. p. 20–42.
[29] Stelzer EHK. Contrast, resolution, pixelation, dynamic range and signal- to-noise ratio: fundamental limits to resolution in fluorescence light microscopy. J Microsc 1998;189:15–24.
[30] Bernas T, Zarebski M, Cook RR, Dobrucki JW, Cook PR. Minimizing photobleaching during confocal microscopy of fluorescent probes bound to chromatin: role of anoxia and photon flux. J Microsci 2004;215(Pt 3):281–96.
[31] Diaspro A, Chirico G, Usai C, Ramoino P, Dobrucki J. Photobleaching. In: Pawley JB, editor. Handbook of Biological Confocal Microscopy SE – 39. New York: Springer, US; 2006. p. 690–702.
[32] Kuang C, Luo D, Liu X, Wang G. Study on factors enhancing photobleaching effect of fluorescent dye. Measurement 2013;46(4):1393–8.
[33] Marcu L, Grundfest WS, Maarek JM. Photobleaching of arterial fluorescent compounds: characterization of elastin, collagen and cholesterol time-resolved spectra during prolonged ultraviolet irradiation. Photochem Photobiol 1999;69(6):713–21.
[34] Song L, Hennink EJ, Young IT, Tanke HJ. Photobleaching kinetics of fluorescein in quantitative fluorescence microscopy. Biophys J 1995;68(6):2588–600.
[35] Vicente NB, Zamboni JED, Adur JF, Paravani EV, Casco VH. Photobleaching correction in fluorescence microscopy images. J Phys Conf Ser 2007;90:012068.
[36] Zhang X, Li Q, Liu J, Sottini S. Chemical mechanism of photobleaching of poly-3BCMU film. J Photochem Photobiol A Chem 1996;95:239–44.
[37] Axelrod D, Koppel DE, Schlessinger J, Elson E, Webb WW. Mobility measurement by analysis of fluorescence photobleaching recovery kinetics. Biophys J 1976;16(9):1055–69.
[38] Ishikawa-Ankerhold HC, Ankerhold R, Drummen GPC. Advanced fluorescence microscopy techniques – FRAP, FLIP, FLAP, FRET and FLIM. Molecules 2012;17(4):4047–132.
[39] a Dunn G, Dobbie IM, Monypenny J, Holt MR, Zicha D. Fluorescence localization after photobleaching (FLAP): a new method for studying protein dynamics in living cells. J Microsci 2002;205(Pt 1):109–12.
[40] Cheng VWT, Screen HRC. The micro-structural strain response of tendon. J Mater Sci 2007;42(21):8957–65.
[41] Patterson GH, Piston DW. Photobleaching in two-photon excitation microscopy. Biophys J 2000;78(4):2159–62.
[42] Sachs C, Fabritius H, Raabe D. Experimental investigation of the elastic-plastic deformation of mineralized lobster cuticle by digital image correlation. J Struct Biol 2006;155(3):409–25.
[43] Zhang D, Eggleton CD, Arola DD. Evaluating the mechanical behavior of arterial tissue using digital image correlation. Exp Mech 2002;42(4):409–16.
[44] Brunon A, Bruyère-Garnier K, Coret M. Mechanical characterization of liver capsule through uniaxial quasi-static tensile tests until failure. J Biomech 2010;43(11):2221–7.
[45] Lanir Y, Salant EL, Foux A. Physico-chemical and microstructural changes in collagen fiber bundles following stretch in vitro. Biorheology 1988;25(4):591–603.
[46] Hannafin JA, Arnoczky SP. Effect of cyclic and static tensile loading on water content and solute diffusion in canine flexor tendons: an in vitro study. J Orthop Res May 1994;12(3):350–6.